Linear unsteady mountain waves

By FRANÇOIS LOTT[*][1] and HECTOR TEITELBAUM, *Laboratoire de Météorologie Dynamique du C.N.R.S., Ecole Polytechnique, 91128 Palaiseau Cedex, France*

ABSTRACT

The object of this paper is to describe the generation of mountain gravity waves when the incident wind is transient. The incident flow is a stably stratified fluid which velocity starts from zero at a given time and returns to zero after a finite time. For the mountain, both a single harmonic and a single ridge topography are considered. The nature of transient effects on the disturbance is discussed according to the value of the parameter, $\varepsilon = U_0 t_f / L$, which measures the ratio between the time scale t_f of the temporal variation of the incident wind and the advective time scale L/U_0. L and U_0 characterize the horizontal extension of the mountain and the incident wind intensity respectively. Situations for which $\varepsilon \gg 1$ are referenced as quasi-steady and the wavefield can be conveniently described using ray-tracing techniques. Situations for which $\varepsilon \ll 1$, are referenced as very unsteady, and essentially reduce to a ground vibrating disturbance generated in a fluid at rest. In this paper, we consider both limit configurations as well as intermediate ones. This allows us to describe various mechanisms of generation of unsteady mountain waves. The incidence of the unsteadiness on the amplitude of the gravity wave momentum flux and on the location of the mountain wave breaking level are also discussed.

1. Introduction

The first comprehensive theoretical description of the atmospheric mountain gravity waves was made in the linear case by Queney (1947) and Scorer (1949). Thereafter, linear and nonlinear studies have been developed in order to give a comprehensive picture of these waves and of the associated severe downslope windstorms occurring in the lee of mountains (Long, 1953; Peltier and Clark, 1979; Durran, 1986; Durran and Klemp, 1987; Klemp and Lilly, 1975; Bacmeister and Pierrehumbert, 1988). These studies typically assume that the incident flow is steady, although some unsteadiness in the wave field can result from the start up of the incident flow (Palm, 1953; Jusem and Barcilon, 1985) or from local instabilities of the main wave (Laprise and Peltier, 1989; Bacmeister and Schoeberl, 1989). Never-

theless, the energy of the disturbance remains transported by a main stationary wave because the incident flow becomes steady after a finite time.

Observations show that this assumption is not always valid. Some atmospheric examples can be found in Buzzi and Tibaldi (1977) which depicts a cold front interacting with a mountain range. More common geophysical examples of transient flow interaction with topography have been studied by oceanographers (Bell, 1975; Hibiya, 1986) in the context of the interaction between the fluctuating tides and the bottom topography (see Maas and Zimmerman (1989) for a review and a complete reference list). In this oceanic context, the mean flow varies as a single harmonic in time, allowing certain simplifications in the mathematical treatment of the problem. Nevertheless, in the atmospheric case, such a temporal structure of the incident flow is not relevant, the time variations induced by the atmospheric tides being small in the troposphere as compared to those induced by synoptic disturbances. This is not true in the upper stratosphere where the daily fluctuations induced by tides and planetary waves of short period may

---

[*] Present affiliation: European Center for Medium Range Weather Forecast, Shinfield Park, Reading, Berkshire RG29AX, ENGLAND.
[1] Corresponding author.

have significant influence on the gravity waves propagating toward the mesosphere. To approach the atmospheric context, Bannon and Zehnder (1985) add a steady component to such a sinusoidally varying flow. Studying the influence of transience on the mountain drag, they found that some evanescent modes, which do not participate in the mountain drag in the steady case (Smith, 1979) can contribute to the instantaneous mountain drag in the unsteady case. Large drag states are then found during the accelerating periods of the flow. In a previous paper (Lott and Teitelbaum, 1993) have investigated theoretically the quasi-steady mountain waves when the time-varying wind is not a single temporal harmonic but when the mountain is a single horizontal harmonic. In order to provide a simple description of the transient effects of the incident wind on the mountain waves, attention was limited to cases for which the incident wind has at most one accelerating phase and one decelerating phase. This was taken as an idealization of winds in situations such as the interaction between a synoptic disturbance and a topography. It is very different from the case of a sinusoidally varying wind where an infinite number of accelerations and decelerations of the incident wind contribute to the wave field. The purpose of the present paper is to extend these previous results to cases for which the mountain has a complex horizontal structure and to cases for which the temporal fluctuation of the incident wind is more rapid.

It is now generally accepted that breaking gravity waves provide a major source of momentum in the atmosphere. They play an important role in the general circulation of the mesosphere (Lindzen, 1981; Holton, 1983). More recently, Schoeberl (1985) and Palmer et al. (1986) have shown that mountain gravity waves are important in the general circulation of the stratosphere and of the upper troposphere respectively. The incidence of these waves on the general circulation of the atmosphere strongly depends on three salient features: their phase velocity, the quantity of momentum they carry and the altitude where they break. In the parametrization scheme of mountain waves presently used in large scale circulation models, the phase velocity of mountain waves is zero and the determination of their breaking level is based on stationary concepts. This can have serious consequences on the incidence of these

waves in the general circulation models. For instance, the assumption of zero phase velocity makes these waves encounter critical level where the large scale flow is zero. This would not occur (or would occur elsewhere) if the phase velocities of the waves were different, as can occur in the unsteady case.

In the present study, we investigate the structure of the mountain gravity waves generated by a transient wind which has one accelerating phase and one decelerating phase. In the second part, the model used is described. In the third part, we study the waves forced on a single horizontal harmonic mountain. This profile is adopted because in many parametrization schemes, the physical background is based on the theory of monochromatic mountain gravity waves. More physically, this type of profile also schematizes a mountain massif, where successive ridges are present. The quasi-steady case is presented in subsection 3.1, where we describe again some of the results found in Lott and Teitelbaum (1993). Subsection 3.2 presents the very unsteady case. In Section 4, we consider a single mountain ridge. In Subsections 4.1 and 4.2 the quasi-steady and the very unsteady cases are presented respectively. In Subsection 4.3, the incidence of the unsteadiness on the breaking level of mountain waves is analysed. All the results are discussed according to the unsteady parameter, $\varepsilon = U_0 t_f / L$, and a particular attention is paid to the horizontal phase velocity of the waves and to the horizontal momentum they carry. The appendixes show analytical results which simplify the interpretation of the simulations presented.

2. Numerical model

We modify the well-known Queney (1947) problem, to allow the spatially uniform incident wind to be a function of time. The model atmosphere is a stably stratified, inviscid, anelastic fluid in a nonrotating reference frame. The basic state velocity field is a zonal wind of the form

$$u_0(t) = U_0 u_v(t),$$

where $U_0 = 20 \text{ ms}^{-1}$. In all the cases considered, the time variation of the wind intensity is given by

$$u_v(t) = \frac{1}{2}\left(1 + \cos\left(\frac{\pi t}{t_f}\right)\right) \qquad \text{for} \quad |t| < t_f$$

$$\text{and} \qquad u_v(t) = 0 \qquad \text{for} \quad |t| > t_f. \tag{1}$$

The wave dynamics is then investigated using a two dimensional (x, z), linear time-dependent model. The stream funcion, Ψ_1, the buoyancy force, φ_1, and the vorticity, ζ_1, associated with the internal wave field are defined by:

$$u_1 = \frac{1}{\rho}\frac{\partial \Psi_1}{\partial z}; \qquad w_1 = -\frac{1}{\rho}\frac{\partial \Psi_1}{\partial x}$$

$$\text{and} \qquad \varphi_1 = g\left(\frac{\theta - \Theta(z)}{\Theta(z)}\right),$$

where

$$\zeta_1 = \frac{\partial u_1}{\partial z} - \frac{\partial w_1}{\partial x} = \frac{1}{\rho}\left(\frac{\partial^2 \Psi_1}{\partial z^2} + \frac{1}{H}\frac{\partial \Psi_1}{\partial z} + \frac{\partial^2 \Psi_1}{\partial x^2}\right). \tag{2}$$

θ is the total potential temperature, $\Theta(z)$ and $\rho(z)$ are the basic state potential temperature and density profiles respectively. In the experiments presented, the density scale height is constant, $H = -\rho/\rho_z = 7000$ m. Then, the equations of motion are written in the streamfunction vorticity form:

$$\left(\frac{\partial}{\partial t} + u_0 \frac{\partial}{\partial x}\right)\zeta_1 + \frac{\partial \varphi_1}{\partial x} + b\zeta_1 + \frac{1}{\rho}\frac{db}{dz}\frac{\partial \Psi_1}{\partial z} = 0, \tag{3}$$

$$\left(\frac{\partial}{\partial t} + u_0 \frac{\partial}{\partial x}\right)\varphi_1 - \frac{N^2}{\rho}\frac{\partial \Psi_1}{\partial x} + b\varphi_1 = 0. \tag{4}$$

Here, $N^2 = 4\ 10^{-4}\text{s}^{-2}$, is the buoyancy frequency and b is a linear damping coefficient. At the bottom boundary, the topographic gravity waves are forced through the condition:

$$\Psi_1(x, z = 0, t) = -\rho(z = 0)\, u_0(t)\, h(x), \tag{5}$$

where the mountain profile, $h(x)$, is characterized by its maximum height $H_0 = 450$ m, and by its width $L = 15$ km. The quite small value of H_0 justifies the use of the linear approximation. In fact, it corresponds to a characteristic Froude number, $Fr = NH_0/U_0 = 0.45 < 1$, for which Long (1953) has shown that the steady nonlinear solution is close to the linear one. In order to prevent undesirable wave reflection at the upper boundary,

a 30-km sponge layer is used. In this layer, the damping coefficient b smoothly increases from zero to $2.5U_0/L$, and the upper boundary condition is,

$$\Psi_1(x, z = z_t, t) = 0.$$

It ensures that no mean transport occurs in addition to the one specified through u_0. In the horizontal direction, we apply periodic boundary conditions. The spatial derivatives in the x and z directions are calculated with centred finite differences. The temporal integration of (3) and (4) are performed using the predictor corrector algorithm used by Lindzen and Barker (1985). The vertical integration of the stream function Eq. (2) is performed with a Gaussian elimination technique.

In Section 3, we consider that the wave is forced by a single harmonic mountain,

$$h(x) = H_0 \cos(kx), \qquad \text{where} \quad k = \pi/L. \tag{6}$$

In the horizontal direction, 32 points are used, and the horizontal period of the domain is $2L$. In the vertical direction, the domain extension is 190 km (including the 30 km sponge layer), the grid is uniform and 512 points are used. Our numerical experiments revealed that these horizontal and vertical resolutions are sufficient for convergence of the solution.

In the Section 4, we consider that the wave is forced by a single ridge mountain,

$$h(x) = \frac{H_0 L^2}{x^2 + L^2}. \tag{7}$$

As we shall see in Section 4, the unsteady mountain waves can propagate rapidly in the horizontal directions. Then, the sizes of the domain are chosen so that most of the windward (leeward) propagating waves can get away the domain through the upper boundary, before re-entering in the domain (and affect the solution by a pseudo-periodic effect) through its leeward (windward) vertical boundary. For this reason, the horizontal domain extension we impose is very large as compared to L: it is 800 km and 640 points are used. In the vertical direction the domain extension is 80 km and 256 points are used. We further verified, that these resolutions are sufficient for the convergence of the solution.

To simplify the comparison of our results with the other studies of mountain waves, we will report them measuring the time in units of t_f, the lengths in units of mountain half width L, the depths in stratification units U_0/N, the momentum flux in units of $\rho(z=0)$ $NU_0H_0^2$, the streamfunction in units of U_0^2/N and the vertical velocity in units of U_0^2/NL.

3. Single harmonic mountain

3.1. Quasi-steady case

In the quasi steady case ($\varepsilon = 43.2$, $t_f = 9$ h), the temporal fluctuations of the incident wind, indicated by t_f, are very slow compared to the advective time scale, $t_a = L/U_0$. This advective time scale also characterizes the rapid fluctuations induced by the wave in the reference frame fixed in regard to the basic flow. This means that the quasi-steady hypothesis is equivalent to the slowly varying hypothesis (Lighthill, 1979) and the propagation of the ground generated waves can be described using ray-tracing techniques. At each initial time t_I, $-t_f < t_I < t_f$, a stationary mountain wave packet is generated at the ground. Its absolute frequency, ω_a, is zero so that its intrinsic frequency, ω_r, is,

$$\omega_r = -ku_0(t_I). \tag{8}$$

Its vertical wavenumber is given by the dispersion relation,

$$m(t_I) = k\left(\frac{N^2}{\omega_r(t_I)^2} - \frac{1}{4k^2H^2} - 1\right)^{1/2}, \tag{9}$$

which is the dispersion relation for internal gravity waves in the anelastic approximation. Thereafter, since the medium doesn't change in z, the vertical wavenumber, m, of the wave packet is conserved (Lighthill, 1979). As m is linked to the intrinsic frequency through the dispersion relation (9), ω_r is also conserved and the wave packet propagates along a straight ray in the (z, t) plane,

$$z = C_{gz}(t_I)(t - t_I),$$

$$\text{where} \quad C_{gz}(t_I) = \frac{-\omega_r(t_I)^3 m(t_I)}{k^2N^2}. \tag{10}$$

Note that the negative value of ω_r (8) ensures that

the ground forced waves propagate upward (10). In Fig. 1, 13 rays are shown for 13 values of t_I, $-t_f < t_I < t_f$. It appears that the (z, t) plane is separated in 3 regions. In the upper region, no wave arrives. In the intermediate region, the solution is the superposition of waves, generated during the ascending phase of the mean flow. The caustic of this system of rays designs, for a given t, the maximum height the ground generated wave packets have arrived: it is the wavefront of the solution. Initially, this front is tangent to the t-axis, indicating a slow initial vertical propagation of the waves. As t increases, this front propagates faster and faster and asymptotically approaches the ray corresponding to the packet of waves generated at $t = 0$, and which intrinsic frequency is, $\omega_{r0} = -kU_0$. In the lower region the solution is the superposition of waves, generated during the ascending phase of the mean flow, and of waves generated during its descending phase.

On Fig. 2, the vertical profile of the function, $\Psi_1 \exp(z/2H)$, and of its amplitude,

$$\langle \Psi_1 \rangle \exp(z/2H)$$

$$= \left(\frac{1}{L}\int_{-L}^{+L} |\Psi_1 \exp(z/2H)|^2 \, dx\right)^{1/2}, \tag{11}$$

are shown at the two different times, $t = 0$, t_f. The multiplicative factor, $\exp(z/2H)$, is introduced to
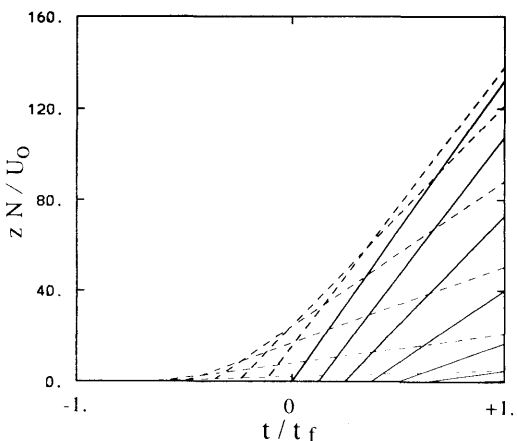

Fig. 1. Rays of wave packet propagation in the (z, t) plane, $\varepsilon = 43.2$ ($t_f = 9$ h). The dashed lines show the packets generated during the ascending phase of the wind; the solid lines show the packets generated during the descending phase of the wind.

suppress the effect of the compressibility in the representation of the solution. Fig. 2 first shows that at each time, the wave field presents well developed oscillations in the vertical direction. This is natural since in the slowly varying context, the characteristic time, t_g, required for the wave energy to propagate over one vertical wavelength, $t_g \approx \lambda_z/C_{gz} \approx 2L/U_0$, is small as compared to t_f: $t_g/t_f \approx 2/\varepsilon \ll 1$. Nevertheless, at $t = 0$ (Fig. 2), the vertical extension of the wavefield is quite small as compared to what happens later ($t = t_f$, Fig. 2). This is due to the slow vertical propagation of the wave packets during the increasing phase of the incident wind. After the incident wind maximum ($t > 0$, Fig. 2), the wavefront, which is

chosen to be the highest maximum of the wave amplitude in the numerical simulation, propagates at $0.8\pi U_0^2/NL = 3.5$ ms^{-1}. This is also consistent with the rays propagation (Fig. 1), the caustic of the rays approximately propagating at the group velocity,

$$C_{gz0} = C_{gz}(\omega_{r0}) = \frac{kU_0^3}{N^2}\left(\frac{N^2}{U_0^2} - \frac{1}{4H^2} - k^2\right)^{1/2}$$

$$\approx \pi \frac{U_0^2}{NL} = 4.2 \text{ ms}^{-1},$$

when $t > 0$. Near the front, the wave amplitude is maximum. This first results from a well known effect of accumulation around caustics in wave dynamics (Lighthill, 1979). When $t > 0$, this also occurs because the waves present at the front were generated at the ground when the wind was nearly maximum. This last effect is indicated on Fig. 1 by the thickness of the rays that is proportional to the wind intensity existing when the wave packets were generated at the ground. Below the wavefront, the solution presents successive bulges and nodes (Fig. 2). It is a signature of the interference between the groups of waves generated during the increasing wind phase with the groups of waves generated during the decreasing wind phase (Fig. 1).

After the wind stops, the horizontal phase velocity is equal to the intrinsic horizontal phase velocity since the background wind is zero. At the front, it is close to $-U_0$ (the intrinsic frequency being close to $-kU_0$). It smoothly approaches 0 when z approaches zero. This vertical variation of the horizontal phase velocity after the wind stops can be indirectly observed on Fig. 2 at $t = t_f$, where the vertical wavelength,

$$\lambda(\omega_r) = 2\pi \left(\frac{k^2N^2}{\omega_r^2} - \frac{1}{4H^2} - k^2\right)^{-1/2}, \tag{12}$$

decreases when z approaches 0. At the front, it is close to $2\pi N/U_0$, it corresponds to a phase velocity, $c \approx -U_0$.

On the Fig. 3, the momentum flux,

$$F_{GW} = \int_{-L}^{+L} \rho u_1 w_1 \, dx \tag{13}$$

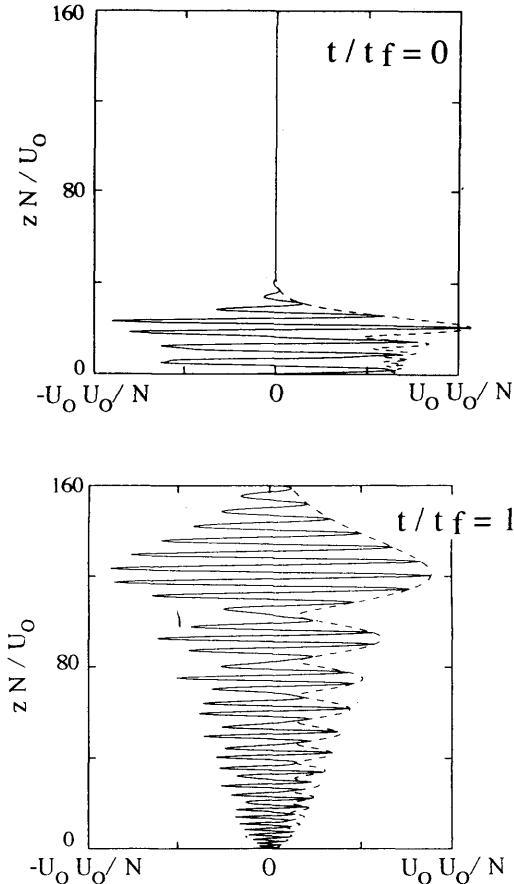carried by the mountain waves is represented as a function of time. It is estimated at the first level of

Fig. 2. Single harmonic mountain, $\varepsilon = 43.2$ ($t_f = 9$ h), time evolution of the function $\Psi_1 \exp(Z/2H)$ (solid line) and of its amplitude $\langle \Psi_1 \rangle \exp(Z/2H)$ (dashed line).

the model (i.e., at $zN/U_0 \approx 0.19$) so that it designes the gravity wave contribution to the instantaneous mountain wave drag. It is compared to the gravity wave drag predicted by the linear stationary theory, this "stationary value" being calculated at each time. As shown on Fig. 3, when the wind starts, this momentum flux increases very slowly as compared to the "stationary" value. This is a natural consequence of the slow initial vertical propagation of the wave field, when only waves of small vertical group velocity are present. Nevertheless, at $t = -0.3t_f$, the momentum flux rapidly increases and attains values exceeding the stationary one. Thereafter, it oscillates suiting the beats described above. Nevertheless, these oscillations are quite small and the "stationary value" remains a very good estimate of the actual momentum flux, as long as the wind blows.

These behaviours of the wavefield and of the wave momentum flux are qualitatively unchanged as long as $\varepsilon \gg 1$, and we further find that the number of bulges present decreases with ε: it approaches 1 when ε approaches 1. For instance, when $\varepsilon = 4.8$ ($t_f = 1$ h, Fig. 4), the vertical profile of the wave field after the wind stops ($t = 2t_f$) contains two bulges, the lowest bulge being very small as compared to the highest one. Furthermore, at the maximum wind ($t = 0$), only one vertical wavelength is present. This is natural since the characteristic time scale, t_g, required for the formation of the wave field over one vertical wavelength, approaches t_f, when ε approaches 1. In this case, the momentum flux (Fig. 3) is significantly lower than its stationary value as long as, $t < -0.5t_f$. This delay, is a signature of the slow formation of the wavefield at the beginning of the wind. Thereafter, and before $t = 0$, all the waves
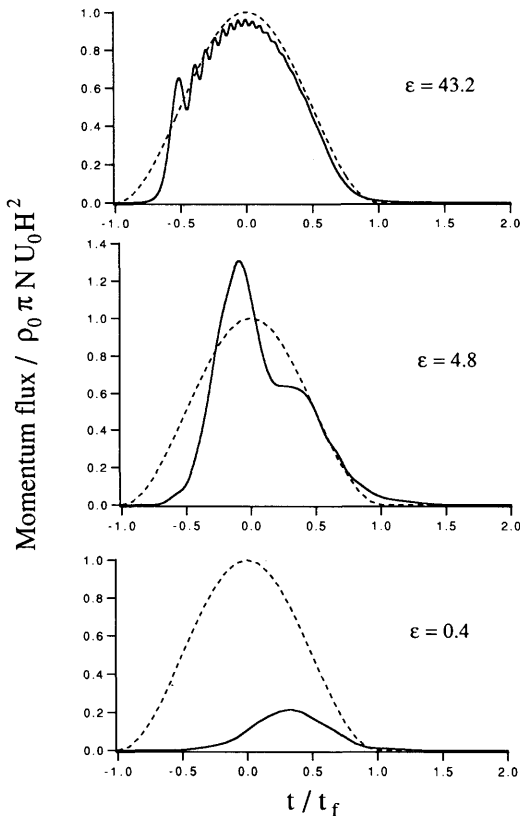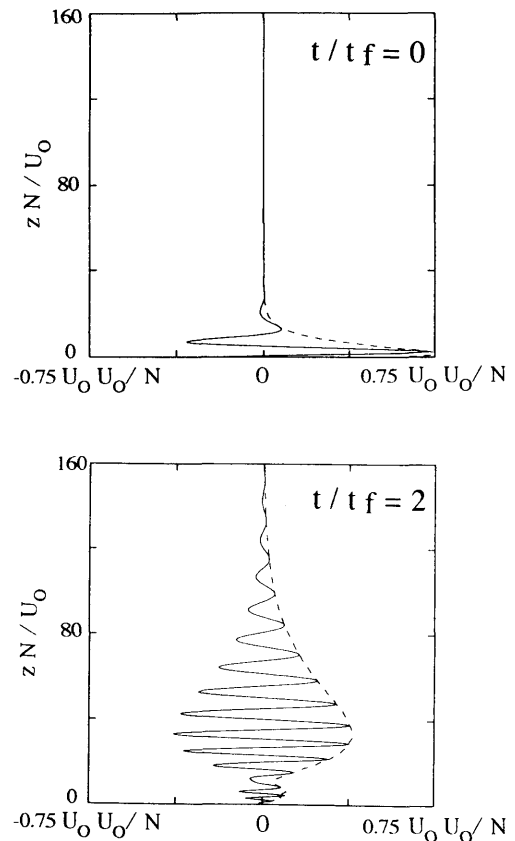

Fig. 3. Single harmonic mountain, normalized gravity wave momentum flux as a function of time. The solid line shows the model estimation at $ZN/U_0 = 0.19$; the dashed line shows the steady estimation.

Fig. 4. Same as Fig. 2 for $\varepsilon = 4.8$ ($t_f = 1$ h).

generated during the increasing wind phase are located just above the topography. This accumulation induces a peak of the momentum flux, which value is 40% larger than the maximum stationary momentum flux. When the node of the wave solution passes, the momentum flux rapidly decreases. According to these results, when $\varepsilon \approx O(1)$, the stationary estimation of the momentum flux is a bad approximation of the actual momentum flux, even if their order of magnitude remain comparable.

3.2. Very unsteady case ($\varepsilon \ll 1$)

In the very unsteady case (Fig. 5, $\varepsilon = 0.4$, $t_f = 300$ s), the temporal variations of the incident wind are rapid as compared to the advective time scale, L/U_0, and the ground generated disturbance has not enough time to develop as a mountain gravity wave when the wind blows. Accordingly, at

Fig. 5. Same as Fig. 2 for $\varepsilon = 0.4$ ($t_f = 5$ min).

$t = 0$, the disturbance is very large near the ground and the sign of the streamfunction, changes at most twice over $25U_0/N$: the scale of this fluctuation differs from the steady mountain wave characteristic wavelength, $\lambda_z \approx 2\pi U_0/N$. Furthermore, the amplitude of the wave field decreases with height and becomes negligible above $25U_0/N$.

After the wind stops ($t = 2t_f$), the disturbance is no longer forced at the ground and disperses in the vertical direction. At this moments, the local vertical wavelength significantly varies over one vertical wavelength. Its characteristic value, which is measured in the middle of the wavefield at $t = 2t_f$ in Fig. 5 is $\lambda_f = 15.7U_0/N$. Accordingly, the radiating waves amplitude and frequency are directly linked to the time Fourier transform of the varying wind. In fact, the characteristic frequency of the ground forcing, $\omega_f = 1/t_f = \varepsilon^{-1}U_0/L \approx 2.5U_0/L$, corresponds to a characteristic wave which vertical wavelength is λ_f. Fig. 5 also shows that the front of the wave system (here chosen as the highest maximum of the wavefield) approximately propagates at the velocity, $28U_0^2/NL = 38 \text{ms}^{-1}$. It is qualitatively coherent with the value of the fastest group velocity, $C_{gz\max} = C_{gz}(\omega_{rs}) = 25U_0^2/NL = 33 \text{ ms}^{-1}$, where $\omega_{rs} = 11.7U_0/L = 1.56 \ 10^{-2}\text{s}^{-1}$, is the inflection frequency for which the vertical group velocity passes by a stationary point:

$$\left(\frac{\partial C_{gz}}{\partial m}\right)_{\omega = \omega_{rs}} = 0.$$

This front propagates nearly $10 \times$ faster than the quasi steady front. Below this front, the wavefield presents successive oscillations which vertical wavelength increases with height at a given time, and decreases with time at a given height. In fact, for the major part of the waves forced at the ground, the vertical group velocity increases with the amplitude of the intrinsic frequency, and with the vertical wavelength. This is due to the fact that in the simulation presented here the inflection frequency, ω_{rs}, is large as compared to the characteristic frequency of the forcing, ω_f. Thus, the waves of largest frequency and vertical wavenumber reach the highest altitude, the other waves remain closer to the ground.

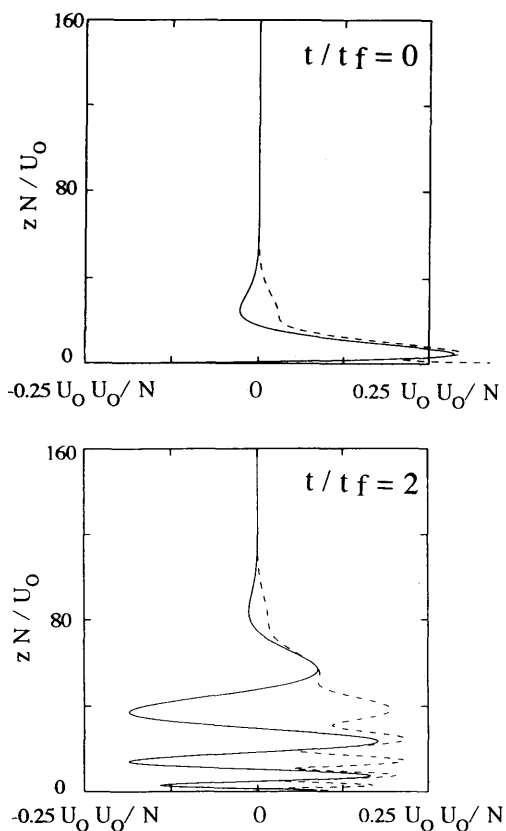Furthermore, as shown on Fig. 5, the wave amplitude has two minima over each vertical

wavelength. At a given time, this can be expressed by writing the square of the wave amplitude as:

$$\langle \Psi_1 \exp(z/2H) \rangle^2 = |A|^2 + |B|^2 + AB^*$$
$$\times \exp(2i\phi(z)) + A^*B \exp(-2i\phi(z)). \qquad (14)$$

Here, ϕ represents the vertical phase of the wave-field, $A(z)$ and $B(z)$ are two functions which varies slowly in the vertical direction as compared to $2\pi/\phi_z$. Since the disturbance is monochromatic in the horizontal direction, it can be written as,

$$\Psi_1 \exp(z/2H) = \text{Real}[C(z) \exp(ikx)],$$

and its amplitude,

$$C(z) = \pm [A \exp(i\phi(z)) + B \exp(-i\phi(z))],$$

according to (11) and (14). This shows that two wave systems of opposite vertical phase are present. Since these two wave systems have opposite vertical wavenumbers, they also have opposite horizontal phase velocities to ensure the upward propagation of energy. This result is opposed to what occurs in the quasi-steady case, where the horizontal phase velocity of the waves is always negative after the end of the wind. It means that in the very unsteady case, no horizontal direction is privileged. This description suggests that the wavefield looks like a ground vibrating distur-bance, generated in a fluid at rest. This last problem is treated analytically in Appendix A, in a simple configuration (Boussinesq + Hydrostatic) allowing analytical treatments. Most wave charac-teristics found in Appendix A, recover the pre-ceding description. Nevertheless, in this section, we only consider a situation for which $\varepsilon = 0.4 < 1$, because in the atmospheric context, it seems unrealistic to consider synoptic wind variations of shorter time scale. As a consequence, the barotropic advection of the wavefield by the mean flow is not exactly negligible and the wavefield simulated also presents some difference with a ground vibrating disturbance in a fluid at rest. For instance, Fig. 5 shows that the wave amplitude does not fall to zero twice by vertical wavelength. The two waves of opposite phase, which amplitude are indicated by A and B in (14), do not have the same amplitude. In this case, the waves with

negative horizontal phase velocity are larger than those with positive horizontal phase velocity. This is important for the momentum flux value. In fact, when a ground vibrating disturbance is generated in a fluid at rest, the momentum flux is zero (see Appendix A), the momentum fluxes carried by waves with positive and negative phase velocity balance. Physically, this compensation occurs because there is no incident flow to be dragged when the background fluid is at rest. In the numerical simulation with $\varepsilon = 0.4$, this momentum flux (Fig. 3) is not exactly zero, the waves with negative horizontal phase velocity being larger than those with positive horizontal phase velocity. Nevertheless, the steady evaluation of the momen-tum flux largely overestimates its actual value (Fig. 3).

In this type of simulation, the reduction of the momentum flux observed, can also be due to the onset of trapped modes with frequency larger than,

$$\omega_T = Nk/(k^2 + \tfrac{1}{4}H^2)^{1/2} = 14.2U_0/L,$$

and which do not contribute to the gravity wave momentum flux. When ε approaches 0, the characteristic frequency of the disturbance, ω_f, increases and approaches ω_T. The proportion of trapped modes in the wavefield increases. In the simulation presented herein, this trapped modes are not important since $\omega_f \ll \omega_T$. Furthermore, Appendix B shows that the reduction of the momentum flux, observed when ε decreases, similarly occurs even when these trapped modes are neglected (i.e., when the Boussinesq and the hydrostatic approximations are both adopted).

4. Single ridge mountain

4.1. Quasi-steady case

For a single ridge mountain, the linear wave solution is a sum of horizontal harmonics such as those presented in Section 3. To determine the rays of propagation of these waves, we consider that the wave packets, associated with each particular zonal harmonic, are generated at the location of the mountain. Then, at each time, $t_1(-t_f < t_1 < t_f)$, a wave packet of intrinsic frequency, $\omega_r = -ku_0(t_1)$, and of a given horizontal wavenumber

k, is generated at the ground. Its trajectory in the (x, z) plane is given by the parametric equations,

$$x = C_{gx}(t_I)(t - t_I) + \int_{t_r}^{t} u_0(s)\, ds, \qquad (15a)$$

$$z = C_{gz}(t_I)(t - t_I),$$

where

$$C_{gx}(t_I) = \frac{\omega_r(t_I)}{k}\left(1 - \frac{\omega_r(t_I)^2}{N^2}\right)$$

$$= -u_0(t_I)\left(1 - \frac{k^2 u_0(t_I)^2}{N^2}\right). \qquad (15b)$$

and $C_{gz}(t_I)$ is given by (10). Nine of these rays, corresponding to 9 values of t_I, are shown on Fig. 6. The horizontal wavenumber is fixed to the characteristic value, $k = 1/L$. Furthermore, the thickness of the rays is proportional to the wind intensity, $u_0(t_I)$. As we consider a long mountain, $U_0/LN = 0.07$, at the time it is generated at the ground, the horizontal intrinsic group velocity nearly balances the mean flow advection, $u_0(t_I)$. Thus, in the steady case, the mountain waves remain located above the topography. Note that for a short mountain, $U_0/LN \approx O(1)$, the intrinsic horizontal group velocity is significantly larger

Fig. 6. Rays of wave packet propagation in the (x, z) plane, $\varepsilon = 43.2$ $(t_f = 9\text{ h})$, $k = 1/L$. The dashed lines show the packets generated during the ascending phase of the wind; the dashed lines show the packets generated during the descending phase of the wind. The numbers characterize the location attained by each packets at the times: (2) $t = -t_f/3$, (3) $t = 0$, (4) $t = t_f/3$, (5) $t = 2t_f/3$, (6) $t = t_f$.

than the opposite of the incident wind, and the waves tend to propagate leeward of the mountain (Queney, 1947). Once generated at the ground the intrinsic group velocity of a wave packet, $C_{gx}(t_I)$, does not change because its intrinsic frequency, $\omega_r(t_I)$, does not change. Nevertheless, as the mean flow changes, this wave packet no longer remains in the vicinity of the mountain. As shown on Fig. 6, the wave packets forced during the ascending wind phase (dashed lines) are first advected leeward since the wind continue to increase after their generation. For this reason, when the incident wind is maximum ($t = 0$, symbol 3 on Fig. 6), all the waves present are slightly located alee of the mountain. This can be seen on Fig. 7, where the stream function is shown at different times. When $t = 0$, the wave pattern is mainly located leeward. For instance, the minima and the maxima of the streamfunction are located in the semiplane ($x > 0$, $z > 0$). Nevertheless, this leeward shift remains slight, because the wave packets which propagate leeward the most efficiently also have the smallest amplitudes. This effect adds to the very large dispersion of these waves, indicated by the initial divergence of the dashed rays in Fig. 6. This leeward shift at $t = 0$, is more evident when the vertical velocity is shown (Fig. 8). In fact, the effect of compressibility tends to enlarge the amplitude of the waves which have reached the highest altitude. At this moment, these waves have been generated at the ground significantly before $t = 0$, and have efficiently experienced the leeward advection described precedingly. Note that this linear mechanism provides an explanation for the generation of lee waves, during the ascending wind phase. After $t = 0$, the incident wind starts to decrease and the largest amplitude waves propagate windward, their advection by the mean flow being smaller than the opposite of their intrinsic group velocity. This windward propagation is first slight, (Fig. 7, $t = \frac{1}{3}t_f$, and symbol 4 on Fig. 6), it becomes very pronounced when $t = \frac{2}{3}t_f$ (Fig. 7 and symbol 5 on Fig. 6). At $t = t_f$ (Fig. 7, and symbol 6 on Fig. 6), the largest waves have left the domain represented and the wave amplitude is small everywhere.
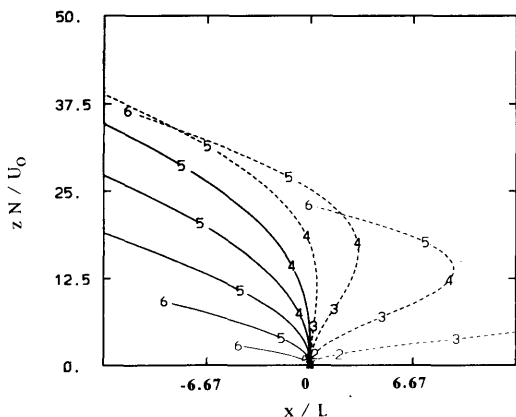
Fig. 9 presents the temporal evolution of the momentum flux,

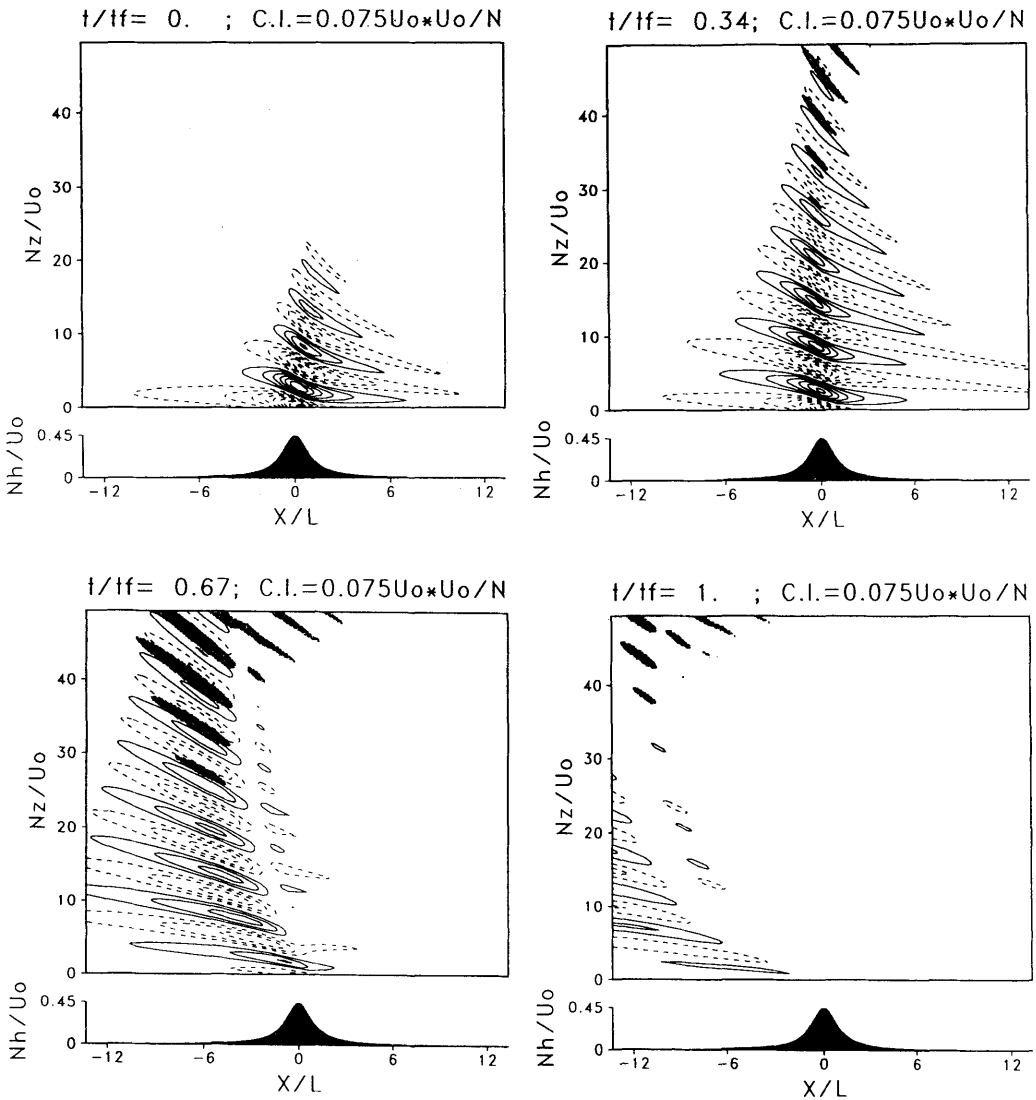$$F_{GW} = \int_{-\infty}^{+\infty} \rho u_1 w_1\, dx.$$

Fig. 7. Single ridge mountain, $\varepsilon = 43.2$ ($t_f = 9$ h). Time evolution of the function $\Psi_1 \exp(Z/2H)$, negative values are dashed and breaking areas are shaded.

As in Section 3, at the beginning of the wind, F_{GW} displays a temporal delay as compared to the steady case. The delay is related to the slow establishment of the wave pattern at the beginning of the wind. Thereafter, the momentum flux is very close from its stationary estimation and contrary to what was found in Subsection 3.1, it does not oscillate. It means that the continuous super-

position of horizontal harmonics, destroy the interference figures observed in Subsection 3.1.

When $\varepsilon = 4.8$ (Fig. 10), the wavefield roughly follows the preceding picture. At $t = 0$, the wave is mostly located above the mountain. As in Subsection 3.1, in the vertical direction the wave field extends over one wavelength: when $\varepsilon \approx O(1)$, the ground forced gravity waves, did not have enough
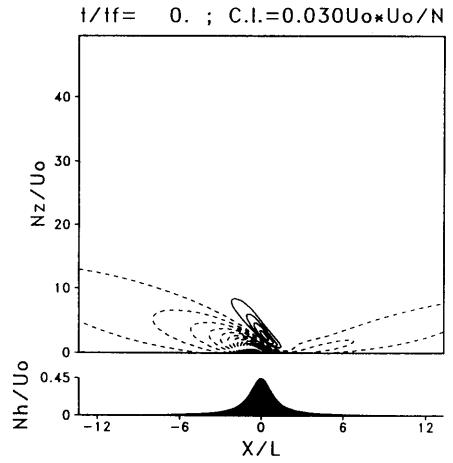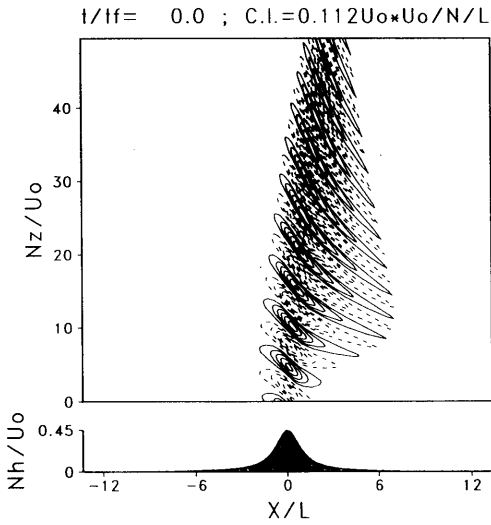
t/tf=   0.0 ; C.I.=0.112Uo*Uo/N/L

Fig. 8. Same as Fig. 7 for the vertical velocity, w_1.

$\varepsilon = 43.2$
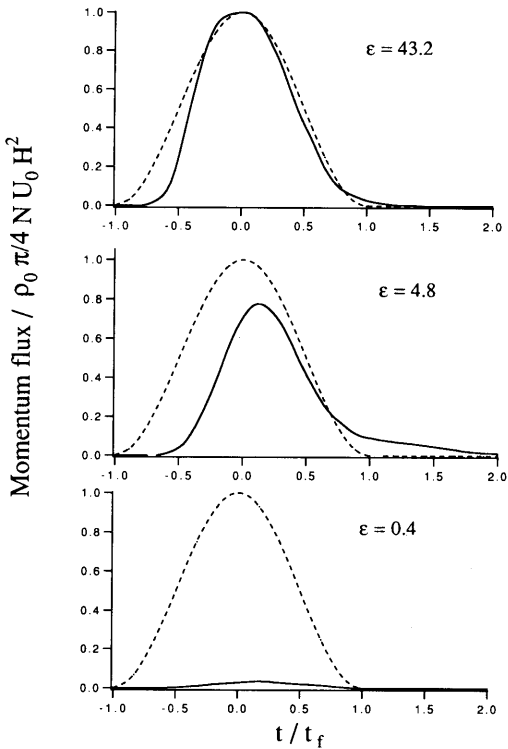
$\varepsilon = 4.8$

$\varepsilon = 0.4$

Fig. 9. Single ridge mountain, normalized gravity wave momentum flux as a function of time. The solid line shows the model estimation at $ZN/U_0 = 0.19$; the dashed line shows the steady estimation.
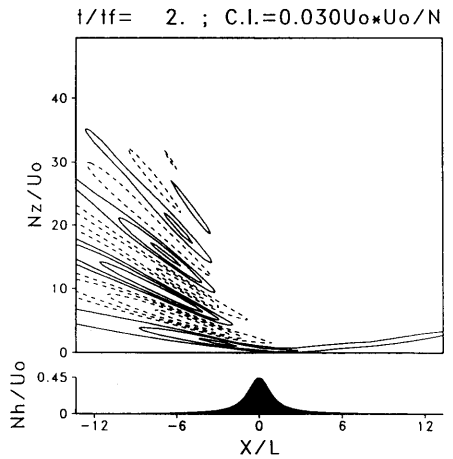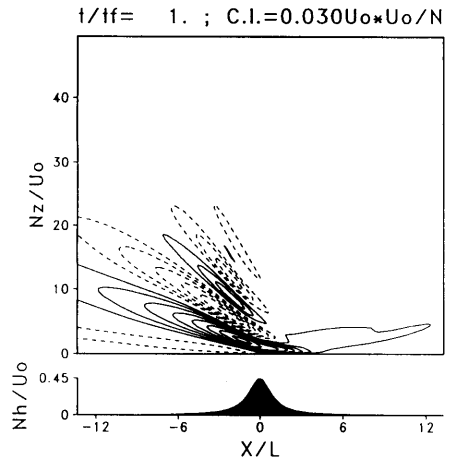
t/tf=   0. ; C.I.=0.030Uo*Uo/N

t/tf=   1. ; C.I.=0.030Uo*Uo/N

t/tf=   2. ; C.I.=0.030Uo*Uo/N

Fig. 10. Same as Fig. 7 for $\varepsilon = 4.8$ ($t_f = 1$ h).

time to develop far above the topography during
the ascending wind phase. As a consequence, the
momentum flux is very lower than its steady value
during the ascending wind phase (Fig. 9). During
the decreasing wind phase, the vertical extension
of the wave enlarges, and the momentum flux
approaches its steady value. After the end of the
wind, the waves propagate windward.

4.2. Very unsteady case

In the very unsteady case (Fig. 11, $\varepsilon = 0.4$), the
wave field is nearly symmetric around $x = 0$. At
$t = 0$, the wavefield is very large near the ground,
its amplitude decreases with height. At this
moment, it did not have enough time to develop as
a mountain gravity wave. Thereafter, the forcing
decreases and ceases rapidly, the induced distur-
bance starts to disperse radiating gravity waves in
both semi-planes $(x > 0)$ and $(x < 0)$. This disper-
sion presents successive "V-shape" pattern similar
to those shown in Mowbray and Rarity (1967),
in which the inclination, relative to the x-axis,
decreases with time. The horizontal wavelength
of the disturbance also decreases with time.
This behaviour can be explained as follows. As
calculated by Bougeault (1983), a gravity waves
field, forced at the ground by a bell-shaped source
oscillating at a given frequency, has a V-shaped
pattern. The wave energy propagates in two
branches, in which the inclinations, relative to the
x-axis, is given by the ratio, C_{gz}/C_{gx}. These
branches are also the branches of constant phase,
because for internal gravity waves, the group
velocity is perpendicular to the phase velocity. This
inclination decreases when the frequency of the
source decreases. In the case considered herein,
the ground forcing is a sum of temporal har-
monics such as those studied by Bougeault (1983).
Furthermore, for the major part of the spectra of
waves generated, the vertical and horizontal group
velocities increase with the frequency and decrease
with the horizontal wavenumber. The waves of
large frequency and small horizontal wave number
propagate away the domain the most rapidly.
Consequently, the solution presents V-shape
pattern in which the inclination and the horizontal
wavenumber decrease with time. This picture is
strictly true when the Boussinesq and hydrostatic
approximations are adopted and when the baro-
tropic advection is neglected. Such a configuration
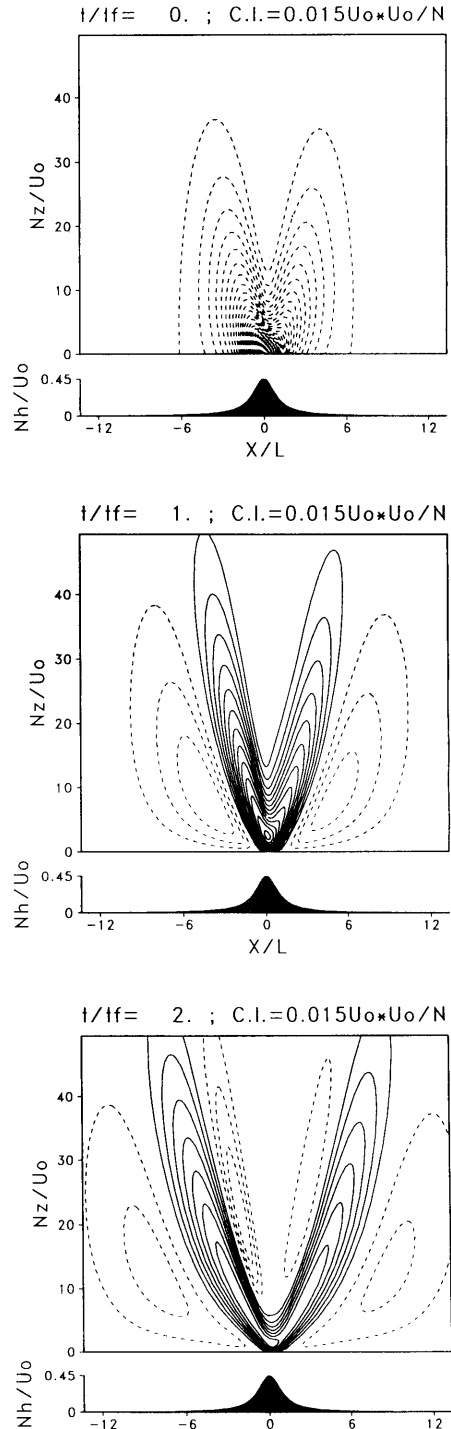is treated analytically in the Appendix A, where

Fig. 11. Same as Fig. 7 for $\varepsilon = 0.4$ ($t_f = 5$ min).

many wave characters observed on Fig. 11, are reproduced.

In the anelastic approximation, the group velocity of the waves possesses a maximum value. Thus, the ground generated disturbance cannot propagate beyond a spatial front which propagation in the (x, z) plane is given by the zeros of the Jacobian $J\{(C_{gx}, C_{gz})/(k, m)\}$, (Lighthill, 1979). Its position is shown on Fig. 12 at different times. As seen comparing Fig. 11 and Fig. 12, the areas designed by the successive fronts (Fig. 12) qualitatively correspond to the areas where the waves are located (Fig. 11). It is reasonable to have a qualitative agreement at this point, since the wave dispersion theory (Lighthill, 1979), is only valid in the slowly varying context or "very far" from the source.

Another difference between the numerical and analytical results, is the small leeward shift of the solution observed on Fig. 11. It is due to the mean flow advection (the basis of the V-shape pattern is located alee of the maximum mountain height). This indicates that the simulation does not strictly reduce to that of a ground vibrating disturbance in a fluid at rest. Nevertheless, the difference remains very small, considering the very small value of the momentum flux (Fig. 9).

4.3. Minimum breaking level

The impact of mountain waves on the large scale flow also depends on the location where they break and deposit the horizontal momentum they carry.
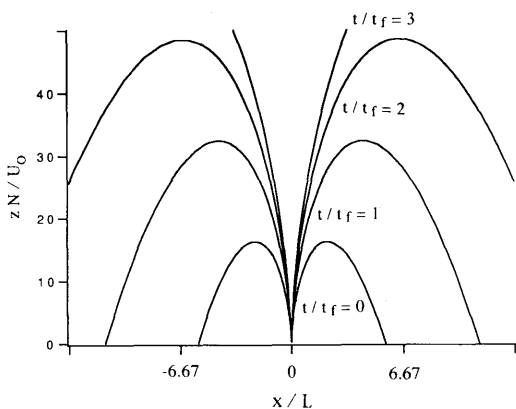

Fig. 12. Theoretical position of the "anelastic" front corresponding to the time dispersion of a ground generated disturbance propagating in a fluid at rest.

Here, the breaking zones correspond to the areas where the total potential temperature, θ, decreases with height (i.e., $\theta_{,z} \leqslant 0$). The wave breaking mechanisms being essentially nonlinear, the linear approach used herein cannot allow to study them in details. Nevertheless, it allows to predict, at least qualitatively, the minimum level of breaking. In the atmosphere, most of the gravity waves generated in the troposphere breaks, because their amplitude (such as the amplitude of the physical quantities u_1, w_1, φ_1) grows with altitude. In the steady case, these quantities grows as $\rho^{-1/2}$ as a consequence of the conservation of the momentum flux with altitude and the minimum level of breaking can be predicted using a stationary WKB analysis (Lindzen, 1981). When the incident wind, U_0, is uniform and when the mountain is a single horizontal harmonic, this stationary value of the minimum breaking level is,

$$Z_{bs} = 2H \ln(U_0/NH_0). \tag{16}$$

When the mountain is a single ridge, the breaking can occur at most one vertical wavelength higher than this value (Schoeberl, 1988). Here we find $Z_{bs} = 17U_0/N$.

Nevertheless, the dispersion of the wave field resulting from the unsteadiness of the flow, has an opposite effect to that of compressibility. This clearly appears in the Figs. 7, 10 and 11. In the steady case, the function, $\Psi_1 \exp(z/2H)$ nearly has a constant amplitude with height. In the unsteady case, the amplitude of the wavefield is the largest at $t = 0$. Thereafter, it disperses vertically and horizontally, its amplitude decreases accordingly. The decrease of the amplitude clearly depends on the duration of the wind. For instance, in the various experiments presented here, we roughly observed that the maximum amplitude of $\Psi_1 \exp(z/2H)$ at $t = t_f$ is two time smaller than its value at $t = 0$. Consequently, the minimum breaking level, raises when ε decreases (Fig. 13). It is close to its steady value when $60 < \varepsilon < 120$. For larger values of ε, the minimum breaking level is lower than its steady value. This is natural since for very large ε, expression (16) can be applied at all times. In this cases, as Z_{bs} decreases with the amplitude of the incident wind, the waves break during the ascending phase of the incident wind. In the range $0 < \varepsilon < 40$, the value of the minimum
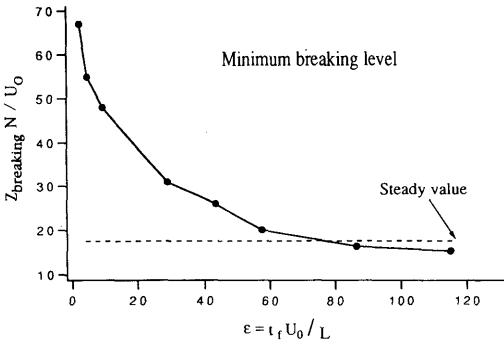
Fig. 13. Single ridge mountain, minimum breaking level as a function of ε.

breaking level increases rapidly with the decrease of ε and reaches ∞, when ε approaches 0.

The location of the breaking areas, which are darken in Fig. 7 and Fig. 8, also deserves comments. At $t = 0$, the waves have not reached sufficiently high altitude and no breaking occurs. At $t = \frac{1}{3}t_f$, the breaking starts to occur above the mountain beyond $z = 35U_0/N$. At this time, the waves that break are not the largest amplitude waves since the area of breaking do not correspond to the area of maximum amplitude of the function, $\Psi_1 \exp(z/2H)$. Therefore, those maximum amplitude waves reach higher altitude and start to break, the altitude of the breaking zone decreases ($t = \frac{2}{3}t_f$). At the same time, the lower breaking zone spreads and is shifted windward following the wave field propagation. At this moment, the lowest breaking area is close from the area of maximum wave amplitude, and the minimum breaking level is found. Thereafter, the lowest breaking area continue to propagate windward along the waves and the minimum breaking level moves upward because the largest amplitude waves propagate upward.

5. Conclusions

We have investigated in some detail the process of internal gravity wave generation by a transient flow of a stably stratified fluid over an obstacle. To isolate the essential physics of the phenomenon, we have retained only the essential elements of a constant density stratification and a simple time dependence in the background flow. For the mountain, we have considered both an infinite single harmonic mountain and a single ridge mountain. Special attention was given to the behaviour of the solution in several important limiting cases, to the unsteadiness of the wavefield, to the estimating of the flux of horizontal momentum and to the minimum breaking level. The results obtained have been found to depend strongly on the parameter $\varepsilon = U_0 t_f/L$, which characterizes the unsteadiness of the incident flow.

When $\varepsilon \gg 1$, the configuration is quasi-steady, and the internal wave field can be described using ray tracing techniques. The wave packets generated at each time at the ground correspond to stationary mountain waves. The unsteadiness of the wavefield then results from the time variation of the ground forcing and from the temporal changes of the background flow occurring after their generation. In the case of a single zonal harmonic mountain ridge, it allows interpretation of the wave structure in terms of the interference between the group of waves generated while the wind lasts. In this case, the wavefront of the solution is the caustic of the rays. Once the wind stops, it propagates at the velocity:

$$C_{gz0} = \frac{\pi U_0^3}{LN^2} \left(\frac{N^2}{U_0^2} - \frac{1}{4H^2} - \frac{\pi^2}{L^2} \right)^{1/2}.$$

The largest waves are located near this front, and their horizontal phase velocity is close to $-U_0$. This indicates that these waves will not encounter critical level at levels of zero mean wind, contrary to what occurs in the stationary theory (Eliassen and Palm, 1960). This is evident in the simulations presented in the present paper, where the waves continue to propagate vertically after the end of the wind. When the mountain is an isolated ridge, the ray tracing technique makes it possible to follow in space the largest amplitude waves. During the ascending phase of the wind, most of the waves propagate leeward of the mountain. Thereafter, they tend to propagate windward. As in the case of a single harmonic mountain, the largest amplitude waves have a phase velocity close to $-U_0$ once the wind stops. Furthermore, the wave field is the superposition of zonal harmonics such as those described precedingly. This superposition destroys the interference pattern existing when the mountain is a single zonal harmonic.

This strong dependence of the wavefield structure on the mountain shape, also has consequences on the temporal evolution of the gravity wave momentum flux. When the wind starts, the momentum flux increases slowly as compared to the incident wind. This is related to the very slow initial establishment of the wavefield in the vertical direction. When the mountain shape is a single harmonic, this flux oscillates as a signature of the interference mentioned above. In some cases, the amplitude of this oscillations becomes large. Then, at a given time the momentum flux can significantly exceed the value estimated by the stationary theory. When the mountain is an isolated ridge these interferences disappear. Furthermore, in all mountain configurations, and when ε approaches 1, it is found that the total momentum carried by the waves, becomes smaller than that predicted by the stationary theory.

When $\varepsilon \ll 1$, we find that the wavefield looks like a ground vibrating disturbance generated in a fluid at rest. When the wind blows, a disturbance is forced at the ground, it has not enough time to radiate away through mountain gravity waves. This disturbance disperses after the end of the wind. When the mountain is a single zonal harmonic, this results in the ground generation of two wave systems of opposite phase velocities. Consequently, the momentum flux carried by the mountain waves is close to 0: the positive flux of momentum carried by waves of positive phase velocity is balanced by the negative flux of momentum carried by waves of negative phase velocity. In this case, the dominant pulsation of the wave field is $\omega_f = 1/t_f$. It corresponds to the dominant temporal harmonic of the ground forcing. Furthermore, the front of the wavefield nearly propagates at the largest group velocity,

$$C_{gz\,\mathrm{max}} = \frac{2\sqrt{3}}{9} \frac{N\pi}{\frac{1}{4}H^2 + \pi^2/L},$$

which is generally very fast as compared to the propagation velocity of the quasi-steady front. When the mountain is a single ridge, the wavefield and the solution presents successive "V-shape" pattern, whose inclination decreases with time. This is due to the rapid energy propagation of the waves of large frequency, which get away from the vicinity of the mountain the most rapidly. As in the case of a single harmonic mountain,

the momentum flux approaches 0 when ε approaches 0.

We also find that the minimum breaking level is very sensitive to ε. Studying a configuration for which the mountain wave breaks in the low stratosphere ($Z_{bs} \approx 17U_0/N$ in the stationary case), we find that it actually breaks significantly above ($\approx 25U_0/N$), when ε is as large as 43.2. Furthermore, the actual minimum breaking level rapidly increases when ε approaches 0. For $\varepsilon > 60$, the minimum breaking level is correctly described by the stationary theory. It is smaller than $17U_0/N$. In this case, the minimum breaking level occurs before the moment of maximum wind. This is natural since the steady breaking level decreases when the wind intensity decreases. In the quasi steady case, we further found that the displacement of the breaking areas partly follows the rays of the largest mountain waves. After the end of the wind, these breaking areas are located far windward of the mountain. It indicates that the momentum transfers between those waves and the mean flow do not occur above the mountain location, contrary to the linear stationary theory.

These results can have important implications for the current gravity wave parameterization schemes used in general circulation models and suggest that such schemes crudely estimate the trajectory and the breaking levels of mountain waves. This study further shows, that in the very unsteady case, the stationary theory gives a bad estimate of the mean flow deceleration by the waves. Nevertheless, in most of the unsteady configurations relevant for atmospheric modelling, the parameter ε is certainly larger than 1. Then, the unsteady structure of the wave field can be described using (time-varying) ray-tracing techniques. Roughly, the momentum flux remains that predicted by the stationary theory. These two results could provide a basis for the improvement of those schemes including non stationary effects. Furthermore, we believe that better parameterization schemes are needed to define more accurately the role of gravity waves in the general circulation of the middle atmosphere. In this context, we presume that the unsteady effects such as those described herein are important. In fact, because of the large vertical extension of the middle atmosphere, and also because of its large stratification, the gravity waves stay a longer time there than in the troposphere. There, they can efficiently

experience the temporal fluctuations of the large scale winds such as those induced by the planetary waves of short period.

6. Appendix A

Disturbance generated by an unsteady ground forcing in a fluid at rest

In this Appendix, we present analytical solutions of a ground generated disturbance in a background fluid at rest. Assuming the hydrostatic approximation and the Boussinesq approximation, the disturbance follows,

$$\frac{\partial^2}{\partial t^2}\frac{\partial^2}{\partial z^2}\Psi_1 + N^2\frac{\partial^2\Psi_1}{\partial x^2} = 0,$$

$$\Psi_1(x, z = 0, t) = -u_0(t)\,h(x). \qquad (A1)$$

Here, the stream function Ψ_1, is related to the vertical and horizontal velocities by,

$$u_1 = \frac{\partial\Psi_1}{\partial z}, \qquad w_1 = -\frac{\partial\Psi_1}{\partial x}.$$

To simplify the Fourier analysis used, the ground forcing temporal variation follows,

$$u_0(t) = U_0\exp(-|t|/t_f).$$

6.1. Single harmonic mountain

When the mountain height varies in the horizontal direction as a single harmonic,

$$h(x) = H_0\,\text{Real}[\exp(+ikx)], \qquad \text{where} \quad k = \pi/L,$$

the stream function is given by,

$$\Psi_1(t, x, z) = \frac{U_0 H_0}{\pi t_f}\,\text{Real}$$

$$\times\left[\int_{-\infty}^{+\infty}\frac{\exp(ikx - i\,((kNz/\omega) + \omega t))}{\omega^2 + t_f^{-2}}\,d\omega\right]. \quad (A2)$$

In (A2), the sign of the vertical wavenumber has been chosen so that each particular modes propagate vertically.

When $t \leqslant 0$, the integral in (A2) has been directly computed using a Fast Fourier Transform algorithm. Suiting conventional techniques, the singular point, $\omega = 0$, has been passed round intro-

ducing a small dissipation in the wave equations. It is shown at $t = 0$, on Fig. 14, and the constant parameters correspond to those used in the "very unsteady" experiment presented in Subsection 3.2. As discussed in the text, the disturbance remain located just above the bottom boundary: the dispersion by internal wave being to slow to compensate the input of energy at the lower boundary.

When $t > 0$, the integral in (A2) can be estimated using the method of the stationary phase (Lighthill, 1979). It indicates that the disturbance starts to differentiate radiating gravity waves of identifiable frequency. Then, the integral equation (A2), admit two stationary points,
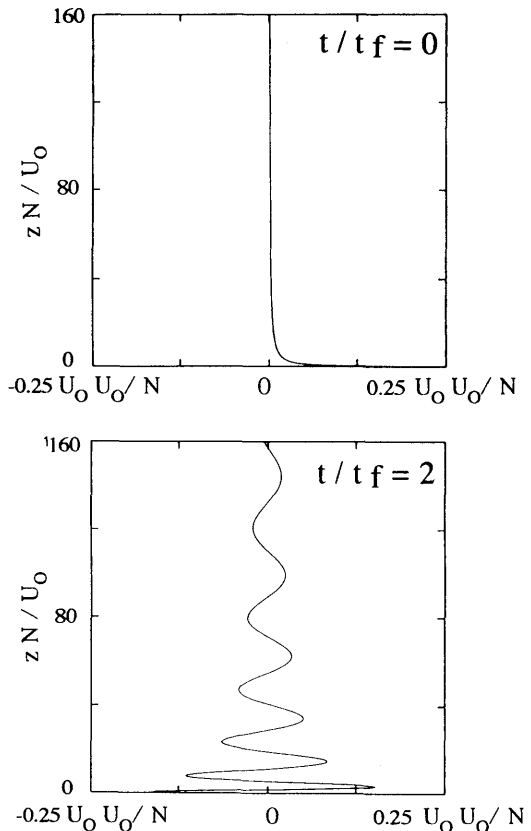
$$\omega_s = \pm\left(\frac{kNz}{t}\right)^{1/2},$$

Fig. 14. Single harmonic mountain, ground generated disturbance in a fluid at rest, $\varepsilon = 0.4$ ($t_f = 5$ min): time evolution of the function Ψ_1. The Boussinesq and hydrostatic approximations are adopted.

and the asymptotic form of (A2), for 'large' z, is (Lighthill, 1979),

$$\Psi_1(t, x, z) = \frac{U_0 H_0}{\pi^{1/2}} \frac{(kNzt)^{1/4}}{kNzt_f + t/t_f},$$

$$\times \text{Real}[\exp(+i((kNzt)^{1/2} + kx + \pi/4))$$

$$+ \exp(-i((kNzt)^{1/2} - kx + \pi/4))]. \quad (A3)$$

Furthermore, the accuracy of this asymptotic form has been verified, by comparing it with the exact solution (A2), estimated with the FFT algorithm mentioned above. The wave field given by (A3) is shown at $t = 2t_f$, in Fig. 14. As seen in (A3), the solution is the superposition of two waves which phase, at a given x, have opposite signs. For each of those waves, the frequency and the vertical wavelength,

$$\omega = \partial_t((kNzt)^{1/2}) = \frac{1}{2}\left(\frac{kNz}{t}\right)^{1/2},$$

$$\lambda_z = 2\pi/\partial_z((kNzt)^{1/2}) = 4\pi\left(\frac{z}{kNt}\right)^{1/2},$$

increase with height. At a given height, these quantities, decrease with time. This is natural since in the context adopted herein, the group velocity of internal waves increasing when the frequency increases, the most rapid waves reach the highest altitude. Note also that this quantities, significantly varies over one vertical wavelength.

Concerning the momentum flux, it can be easily seen in equation (A2) that the function Ψ_1, is symmetric relatively to $x = 0$. Consequently, u_1 is also symmetric but w_1 is antisymmetric, and the momentum flux (13), $F_{GW} = 0$.

6.2. Single ridge ground forcing

When the ground forcing intensity varies in the horizontal direction as a single ridge (7), the analytical form of the stream function is

$$\Psi_1 = \frac{1}{2\pi}\int_{-\infty}^{+\infty}\int_{-\infty}^{+\infty} \frac{H_0 L U_0}{t_f} \frac{\exp(-|k|\,L)}{\omega^2 + t_f^{-2}}$$

$$\times \exp\left(i\left(kx - \frac{kNz}{\omega} - \omega t\right)\right) dk\, d\omega. \quad (A4)$$

Here again, the sign of the vertical wavenumber is chosen so that each harmonic propagates upward.

It is noteworthy that (A4) can be calculated exactly. When $t \leqslant 0$, the stream function (A4) is given by,

$$\Psi_1(t, x, z) = \frac{H_0 L}{t_f} u_0(t)(x^2 + L^2)$$

$$\times \frac{Nz + L/t_f}{N^2 z^2 x^2 + (NzL + (x^2 + L^2)/t_f)^2}. \quad (A5)$$

This is shown at $t = 0$, in Fig. 15. As in the preceding case, as long as $t < 0$, the disturbance does not present a wave structure. When $t > 0$, the stream function (A4) is given by

$$\Psi_1(t, z, z) = \frac{H_0 L}{t_f} u_0(t)(x^2 + L^2)$$

$$\times \frac{Nz - L/t_f}{N^2 z^2 x^2 + (NzL - (x^2 + L^2)/t_f)^2}$$

$$- \frac{\left(\begin{array}{c} 2\dfrac{H_0 L Nz}{t_f} u_0\left(\dfrac{NzLt t_f}{x^2 + L^2}\right) \\ \times \left\{(N^2 z^2 - (L^2 - x^2)/t_f^2)\cos\left(\dfrac{Nzxt}{x^2 + L^2}\right)\right. \\ \left. - 2Lx/t_f^2 \sin\left(\dfrac{Nzxt}{x^2 + L^2}\right)\right\} \end{array}\right)}{N^4 z^4 - 2N^2 z^2(L^2 - x^2)/t_f^2 + (L^2 + x^2)^2/t_f^2}.$$

$$(A6)$$

This is shown at $t = t_f$, $2t_f$, in Fig. 15. The first right-hand term in (A6) is very close to that found when $t \leqslant 0$ (A5). It corresponds to the part of the disturbance which continues to be forced at the ground and which has not enough time to disperse through gravity waves. This part rapidly decreases since its amplitude is directly linked to the decreasing forcing intensity, $u_0(t)$. The second part corresponds to the dispersing internal wave field. Even if its structure is very complex, it is possible to recognize a phase, ϕ,

$$\phi(x, z, t) = \frac{Nzxt}{x^2 + L^2}.$$

In this case, the frequency increases with height, and the vertical wavenumber decreases with time. The "V-shape" pattern of the solution, can be
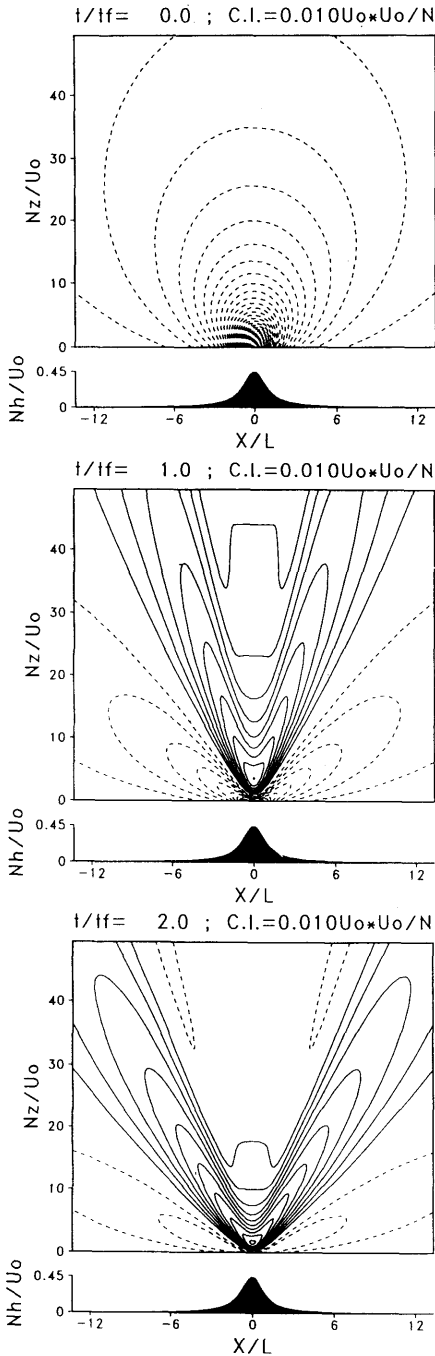
Fig. 15. Single ridge mountain, ground generated disturbance in a fluid at rest, $\varepsilon = 0.4$ ($t_f = 5$ min): time evolution of the function, Ψ_1. Negative values are dashed. The Boussinesq and hydrostatic approximations are adopted.

characterized by the lines of constant phase. For large x, these are given by,

$$\frac{Nzt}{x} \approx \text{const},$$

and their inclination relatively to the x-axis decreases with time, as observed on Fig. 15. This is a signature of the rapid evacuation of the waves of large frequency.

Concerning the momentum flux, it can be easily seen in equation (A4) and (A5), that the function Ψ_1, is symmetric relatively to $x = 0$. Consequently, u_1 is also symmetric and w_1 is antisymmetric. Thus, the momentum flux (13), $F_{GW} = 0$.

7. Appendix B

Momentum transfer

As in Appendix A, we assume the hydrostatic and the Boussinesq approximations, but the mean flow advection is no longer neglected in the internal wave equation and the incident flow is given by (1). When the mountain is a single zonal harmonic, $h = \text{Real}(H_0 \exp(ikx))$, the stream function, $\Psi_1 = \text{Real}(\hat{\Psi} \exp(ikx))$, is given by the equations,

$$\left(\frac{\partial}{\partial t} + iku_0(t)\right)^2 \frac{\partial^2}{\partial z^2} \hat{\Psi} + N^2 \frac{\partial^2 \hat{\Psi}}{\partial x^2} = 0,$$

$$\hat{\Psi}(z = 0, t) = -u_0(t) H_0. \qquad (B1)$$

Following Bell (1975), we solve (B1) in the reference frame fixed with respect to the basic flow. This is done by introducing the function, $\tilde{\Psi}$,

$$\tilde{\Psi} = \hat{\Psi} \exp\left(ik \int_0^t u_0(s)\,ds\right).$$

Then, (B1) becomes,

$$\frac{\partial^2}{\partial t^2} \frac{\partial^2}{\partial z^2} \tilde{\Psi} - N^2 k^2 \tilde{\Psi} = 0,$$

$$\tilde{\Psi}(z = 0, t) = -u_0(t) H_0 \exp\left(ik \int_0^t u_0(s)\,ds\right).$$
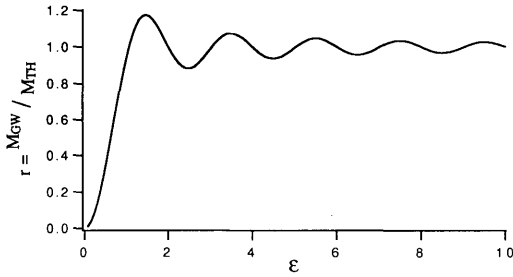
Fig. 16. Ratio between the actual momentum flux and its steady estimation as a function of ε. The Boussinesq and the hydrostatic approximations are adopted.

In this reference frame, the wavefield, $\tilde{\Psi}$, can be solved as the sum of monochromatic waves, which frequency, ω, and vertical wavenumber, m, satisfy the dispersion relation, $m = -kN/\omega$. Returning to the reference frame fixed with respect to the topography, the final solution writes:

$$\Psi_1 = \text{Real}\left[\exp\left(-ik \int_0^t u_0(s)\, ds \right) \right.$$

$$\left. \times \int_{-\infty}^{+\infty} F(\omega) \exp\left(i\left(kx - \omega t - \frac{N}{\omega} kz \right) \right) d\omega \right],$$

$$\tag{B3}$$

where $F(\omega)$ characterizes the amplitude and the initial phase of the mode of frequency, ω:

$$F(\omega) = \frac{1}{2\pi} \int_{-\infty}^{+\infty} -u_0(t)\, H_0$$

$$\times \exp\left(+ik \int_0^t u_0(s)\, ds + i\omega t \right) dt. \tag{B4}$$

Similarly, the horizontal and vertical velocity, u_1 and w_1, can be calculated, replacing $F(\omega)$ in (B3), by $Nk/\omega F(\omega)$ and $-ikF(\omega)$, respectively. These velocities can then be computed using a Fast Fourier Transform algorithm close to the one used in Appendix A. Then, the momentum F_{GW} (13), is calculated at $z = 0$ and the total momentum M_{GW} carried by the waves during the wind,

$$M_{\text{GW}} = \int_{-t_f}^{+t_f} F_{\text{GW}}\,(z = 0, t)\, dt,$$

is estimated and compared to that predicted by the stationary theory, this theory being applied at each moment:

$$M_{\text{th}} = \int_{-t_f}^{+t_f} \rho_0 \pi N H_0^2 u_0(t)\, dt = t_f \rho_0 \pi N H_0^2 U_0.$$

The ratio between this quantities is shown on Fig. 16, as a function of the parameter ε. When ε decreases below 1, and approaches 0, this ratio rapidly falls to zero, the wavefield approaching the configuration of a ground-generated disturbance propagating in a fluid at rest studied in Appendix A.

REFERENCES

Bacmeister, J. T. and Schoeberl, M. R. 1989. Breakdown of vertically propagating two-dimensional gravity waves forced by orography. *J. Atmos. Sci. 46,* 2109–2134.

Bacmeister, J. T. and Pierrehumbert, R. T. 1988. On high drag states of nonlinear stratified flow over an obstacle. *J. Atmos. Sci. 45,* 63–80.

Bannon, P. R. and Zehnder, J. A. 1985. Surface pressure and mountain drag for transient airflow over a mountain ridge. *J. Atmos. Sci. 42,* 2454–2462.

Bell, T. H. 1975. Lee waves in stratified flows with simple harmonic time dependence. *J. Fluid Mech. 67,* 705–722.

Bougeault, P. 1983. A non-reflective upper boundary condition for limited height hydrostatic models. *Monthly Weather Review 111,* 420–429.

Buzzi, A. and Tibaldi, S. 1977. Inertial and frictional effects on rotating and stratified flow over topography. *Quart J. Met. Soc. 103,* 135–150.

Durran, D. R. 1986. Another look at downslope windstorms. Part I: The development of analogs to supercritical flow in an infinitely deep, continuously stratified fluid. *J. Atmos. Sci. 43,* 2527–2543.

Durran, D. R. and Klemp, J. B. 1987. Another look at downslope winds Part II: Nonlinear amplification beneath wave-overturning layers. *J. Atmos. Sci. 44,* 3402–3412.

Eliassen, A. and Palm, E. 1960. On the transfer of energy in stationary mountain waves, *Geophys. Norv. 22,* 1–23.

Hibiya, T. 1986. Generation mechanism of internal waves by tidal flow over a sill, *J. Geophys. Res. 91,* 7697–7708.

Holton, J. R. 1983. The influence of gravity wave breaking on the general circulation of the middle atmosphere, *J. Atmos. Sci. 40,* 2497–2507.

Jusem, J. C. and Barcilon, A. 1985. Simulation of moist,

mountain waves with an anelastic model. *Geophys. Astrophys. Fluid Dynamics 33*, 259–276.

Klemp, L. B. and Lilly, D. K. 1975. The dynamics of wave-induced downslope winds. *J. Atmos. Sci. 32*, 320–339.

Laprise, R. and Peltier, W. R. 1989. The structure and energetics of transient eddies in a numerical simulation of breaking mountain waves. *J. Atmos. Sci. 46*, 565–585.

Lighthill, M. J. 1979. *Waves in fluids.* Cambridge University Press.

Lindzen, R. S. 1981. Turbulence and stress due to gravity wave and tidal breakdown. *J. Geophys. Res. 86*, 9707–9714.

Lindzen, R. S. and Barker, J. W. 1985. Instability and wave overreflection in stably stratified shear flow, *J. Fluid Mech. 151*, 189–217.

Long, R. R. 1953. Some aspects of the flow of stratified fluids. I. A theoretical investigation. *Tellus, 5*, 42–58.

Lott, F. and Teitelbaum, H. 1993. Topographic waves generated by a transient wind. *J. Atmos., Sci.*, in press.

Maas, L. R. and Zimmerman, J. T. F. 1989. Tide-topography interactions in a stratified shelf sea I. Basic equations for quasi-nonlinear internal tides. *Geophys. Astrophys. Fluid Dynamics 45*, 1–35.

Mowbray, D. E. and Rarity, S. H. 1967. A theoretical and experimental investigation of the phase configuration of internal waves of small amplitude in a density stratified fluid. *J. Fluid Mech. 28*, 1–16.

Palm, E. 1953. On the formation of surface waves in a fluid flowing over a corrugated bed and on the development of mountain waves. *Astroph. Norv. 5*, no. 3.

Palmer, T. N., Shutts, G. J. and Swinbank, R. 1986. Alleviation of a systematic westerly bias in general circulation and weather prediction models through an orographic gravity wave drag parametrization. *Quart J. Met. Soc. 112*, 1001–1039.

Peltier, W. R. and Clark, T. L. 1979. The evolution and stability of finite-amplitude mountain waves. Part II: Surface drag and severe downslope windstorms. *J. Atmos. Sci. 36*, 1498–1529.

Queney, P. 1947. *Theory of perturbations in stratified currents with application to airflow over mountains.* Misc. Report no. 23. University of Chicago Press, 81 pp.

Schoeberl, M. R. 1985. The penetration of mountain waves into the middle atmosphere. *J. Atmos. Sci. 42*, 2856–2854.

Schoeberl, M. R. 1988. A model of stationary gravity wave breakdown with convective adjustment. *J. Atmos. Sci. 45*, 980–992.

Scorer, R. S. 1949. Theory of waves in the lee of mountains. *Quart J. Met. Soc. 75*, 41–56.

Smith, B. S. 1979. The influence of the earth's rotation on mountain wave drag. *J. Atmos. Sci. 36*, 177–180.